Sunlight-Reduced Graphene Oxides as Sensitive Moisture Sensors for Smart Device Design

Dong-Dong Han, Yong-Lai Zhang, Jia-Nan Ma, Yan Liu, Jiang-Wei Mao, Chang-Hao Han, Kai Jiang, Hong-Ran Zhao, Tong Zhang, Huai-Liang Xu, and Hong-Bo Sun*

Here, a facile fabrication of graphene-based humidity sensors is reported for smart device design. Focused sunlight photoreduction of graphene oxide (GO) helps to remove most of the oxygen-containing groups on GO sheets, which not only recovers their conductivity but also leads to the formation of a highly porous nanostructure, enabling the manufacture of versatile humidity-sensing smart devices, such as moisture controllers, humidity detector robots, and even a novel electronic harmonica, through a very simple technique. As an uncomplicated and chemical-free method, focused sunlight photoreduction of GO provides an avenue to produce versatile sensing devices for the development of smart devices.

1. Introduction

Smart devices that can quickly and decisively respond to environmental stimuli have attracted increasing research interest because they are very promising for future applications in automatic systems and robotics.[1] As a core component of typical smart devices, sensors play a critical role in recognizing environmental changes.[2] Thus, robust sensing devices with high sensitivity, reliability, rapid responses, and long-term durability are highly desired.[3] Taking humidity sensing as an example, to meet sensitivity requirements, new methods have been sought to improve existing sensors based on various transduction techniques and novel materials.[4] In the pursuit of ideal humidity-sensing materials, 2D graphene and related materials (e.g., graphene oxide, GO) have emerged as promising candidates because they show enticing physical/chemical properties (e.g., tunable electrical property,[5] mechanical flexibility,[6] and a large surface to volume ratio[7]) and have broad applications (e.g., energy conversion,[8] smart robots,[9] and biomedical devices[10]). Recently, Ariga and co-workers achieved highly selective gas sensing using ionic liquid-intercalated graphene layers that were prepared by in situ reduction of graphene oxide layers in the presence of nonvolatile ionic liquids, and subsequent electrostatic layer-by-layer assembly.[11] Sadasivuni et al. presented the layer-by-layer spraying of modified graphene oxide-filled cellulose nanocrystals for proximity sensing.[12] Wang et al. reported ultrathin reduced graphene oxide (RGO) films with controllable thicknesses for noncontact relative humidity (RH) sensing.[13] In our previous works, an RGO with hierarchical micro-nanostructures prepared by two-beam-laser interference was employed to produce humidity-sensing devices.[14] However, in spite of these advancements, graphene-based sensing devices have not been well employed for smart device design. A possible reason for this gap would be the difficulty in tailoring highly permeable graphene nanostructures that permit spontaneous, timely, and reliable molecular discrimination. Moreover, complex experimental procedures or special instruments are generally necessary in device fabrication, which largely limits their integration with other devices. The current trend is to produce smart devices equipped with versatile sensors created in facile, reliable, cost-effective, and environmentally friendly manners. However, it is currently challenging to achieve this goal.

Herein, we report a facile preparation of a graphene-based moisture detector for smart device design. A humidity-sensing device has been fabricated by a simple focused sunlight treatment of GO. The drastic removal of oxygen-containing groups (OCGs) not only mediates the controllable tuning of conductive properties but also leads to the formation of a highly porous RGO structure that is of benefit to the adsorption of molecules and humidity sensitivity. The RGO-based humidity-sensing device shows moisture recognition capability and excellent sensing performance, including high sensitivity, good repeatability, small humidity hysteresis, and fast response recovery at room temperature, enabling a series of humidity-sensing devices including a moisture controller, a humidity detector robot, and even a novel electronic harmonica. As a simple and chemical-free method, sunlight-mediated photoreduction of GO provides a very simple and cost-effective way to integrate humidity sensors in the development of versatile moisture-responsive smart devices.

D.-D. Han, Prof. Y.-L. Zhang, J.-N. Ma, J.-W. Mao, C.-H. Han, Dr. K. Jiang, H.-R. Zhao, Prof. T. Zhang, Prof. H.-L. Xu, Prof. H.-B. Sun
State Key Laboratory on Integrated Optoelectronics
College of Electronic Science and Engineering
Jilin University
2699 Qianjin Street, Changchun 130012, China
E-mail: yonglaizhang@jlu.edu.cn
Prof. Y. Liu
Key Laboratory of Bionic Engineering (Ministry of Education)
Jilin University
Changchun 130022, China
Prof. H.-B. Sun
College of Physics
Jilin University
Jiefang Road 119, Changchun 130023, China

DOI: 10.1002/admt.201700045

2. Results and Discussion

Figure 1 shows the schematic diagram and photographs of the experimental procedures for the fabrication of humidity sensors through focused sunlight-induced photoreduction of GO and illustrates their potential applications for smart device design. Briefly, a GO aqueous solution was first dropped and coated on a substrate that contained a pair of electrodes. Subsequently, incident solar radiation was focused on the surface of the GO film using a general convex lens to trigger the photoreduction reaction. The insets of Figure 1a show photographs of the GO film before and after sunlight reduction. Notably, the photoreduction of the GO films occurred as soon as the focused sunlight irradiated the GO film, which could be demonstrated by the rapid color change from yellow-brown to black at precise locations. The photoreduction mechanism could be classified into photochemical and photothermal effects that further depend on the wavelength of incident light. According to the threshold for GO reduction, photon energies larger than 3.2 eV ($\lambda < 390$ nm) could trigger GO reduction through a photochemical process,[15] whereas light irradiation with wavelengths larger than 390 nm could reduce GO due to the photothermal effect. In the case of sunlight, its wavelengths cover a broad spectral range from UV to IR (from ≈295 to 2500 nm), in which the IR region is the primary contributor to the reduction of GO, through the photothermal effect, and the UV light also contributes to the reduction of GO, through the photochemical effect.[16] To tune the intensity of the sunlight irradiation, experiments could be performed for different periods or with the help of a gray glass. In our work, we performed the photoreduction experiments under different solar radiation intensities (≈570 and 710 μW cm^{-2}). The RGO sensor prepared in this way could be directly employed for smart device design (Figure 1, right part).

The photoreduction of GO under sunlight irradiation has been well elucidated, as reported in some previous studies.[17] However, most of these works focused on the photochemical reduction of GO in aqueous solution or the recovery of conductivities; less attention has been paid to the formation of porous structures and the tuning of the reduction degree for sensing applications. In this work, we carefully investigated the photoreduction-induced nanostructuring effect that benefits sensing devices. Both pristine GO and sunlight-reduced RGO samples have been characterized by scanning electron microscopy (SEM). **Figure 2** displays the surface and section images of GO, RGO-1 (reduced at 570 μW cm^{-2}), and RGO-2 (reduced at 710 μW cm^{-2}) films. It is quite apparent that the surface of the pristine GO film is relatively smooth with randomly distributed wrinkles (Figure 2a); the cross-sectional view of the GO film (≈5 μm) reveals a layered nanostructure, which is formed due to the stack of individual GO sheets (Figure 2b), as evidenced from the X-ray diffraction (XRD) patterns (Figure S1, Supporting Information). In contrast, after sunlight reduction at 570 μW cm^{-2}, the surface of the RGO-1 film became rough (Figure 2c), and an expanded structure with large gaps between adjacent RGO sheets could be observed (Figure 2d, see Figure S1 in the Supporting Information). The formation of the expanded structures could be attributed to the photoreduction-induced elimination of OCGs. Interestingly, when the solar radiation intensity was further increased to 710 μW cm^{-2}, the resultant RGO-2 film became highly porous. As shown in Figure 2e,f, the surface of RGO-2 cracked and abundant gaps could be identified all over the surface. The cross-sectional SEM image shows that the stacked layered structure had been converted into well-exfoliated porous structures due to the drastic removal of the OCGs and the emission of carbon species

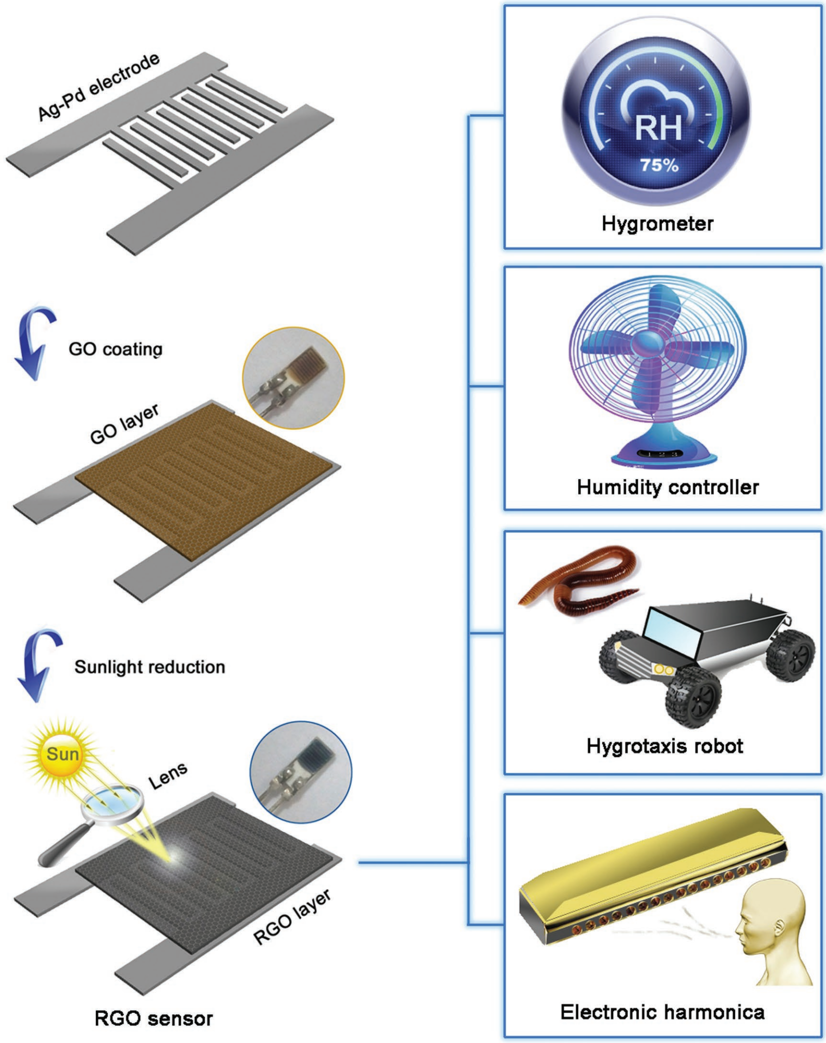

Figure 1. Schematic illustration of the fabrication process of RGO humidity sensors and their potential applications for smart device design.

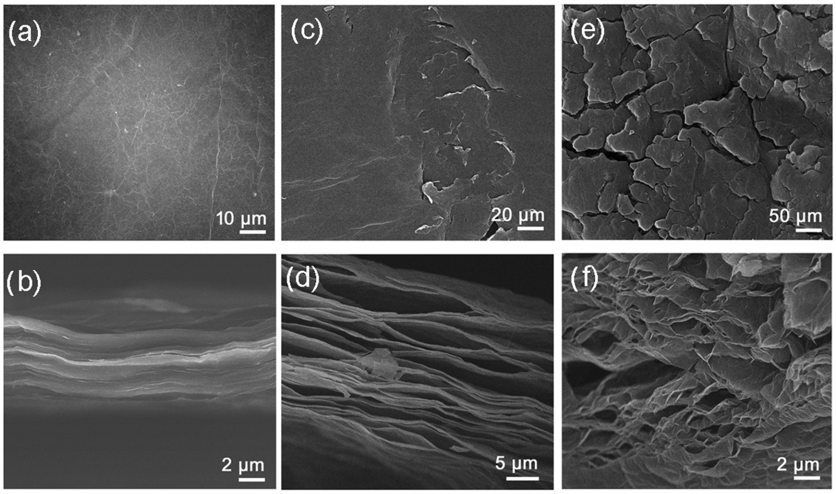

Figure 2. Surface and profile SEM images of the a,b) GO, c,d) RGO-1, and e,f) RGO-2 samples. RGO-1 and RGO-2 films were prepared by sunlight reduction under the average solar radiation intensity of 570 and 710 μW cm^{-2}, respectively.

(e.g., CO, CO_2). Since the whole experiment was carried out at ambient conditions, the presence of oxygen in the air would promote the elimination of OCGs, and thus, a devastating deoxygenation occurred, leading to the formation of such a highly porous structure. It is worth noting that the porous structure would significantly increase the surface area of the RGO sample and accordingly promote the adsorption of gas molecules.

Raman spectroscopy was employed to gain in-depth insight into the structural evolution of these GO and RGO samples (**Figure 3**a). Both GO and RGO films show two prominent peaks at 1354 and 1587 cm^{-1}, corresponding to the D band and G band of graphene, respectively. The D band is associated with the presence of edges and the isolated defects in the structure, and the G peak results from the E_{2g} vibrational mode of sp^2 carbon. Generally, the removal of OCGs from GO sheets would eliminate the majority of the defects and thus lead to a significant decrease in the D band in Raman spectra. However, in our experiment, there is no notable difference between the I_D/I_G ratios of the GO and RGO samples. These results suggest that the focused sunlight irradiation could not recover the sp^2 structure of graphene; it causes additional defects during the drastic removal of OCGs. Since the GO sheets were cracked into small pieces due to the drastic degassing process (see the cracks in Figure 2e), additional defects, mainly dangling bonds on the edges of the GO sheets, were unavoidably generated. In this regard, the resultant RGO material is not suitable for graphene-based devices that require high carrier mobility (e.g., Field-effect-transistors, FETs). However, the presence of defects would make this type of RGO very sensitive to environment.

To evaluate the oxygen residuals of GO films before and after sunlight reduction, thermogravimetric (TG) analysis was performed under N_2 atmosphere (Figure 3b). According to the TG curves, GO shows a weight loss of ≈7% at ≈100 °C due to water removal and a second weight loss of approximately another 33% in the temperature range from 150 to 300 °C due to the loss of OCGs such as carboxyl, hydroxyl, and epoxy groups. Compared with GO, the RGO samples show much less weight loss during thermal treatment. The weight loss at 250 °C is only ≈20% and ≈5% for the RGO-1 and RGO-2 samples, respectively. These results confirm that most of the unstable OCGs were removed during sunlight reduction.

To quantitatively evaluate the reduction degree of the RGO samples, we used X-ray photoelectron spectroscopy (XPS) to measure the oxygen residuals. As shown in Figure 3c, the survey spectra exhibit C1s (≈284 eV) and O1s (≈532 eV) peaks in both the GO and RGO samples. Compared with GO, the O1s peak intensity of the RGO samples significantly decreased after sunlight photoreduction, demonstrating the loss of OCGs. The carbon/oxygen atomic ratios (C/O) of pristine GO and the resultant RGO-1 and RGO-2 samples were calculated to be 1.99, 2.95, and 4.95, respectively. The C1s XPS spectra (Figure 3d) of the GO and RGO samples were fitted with three Gaussian–Lorentzian peaks associated with three different chemical environments of carbon atoms, including nonoxygenated carbon (C—C/C=C, 284.7 eV), hydroxyl and epoxy carbon (C in C—O bonds, 286.8 eV), and carbonyl carbon (C=O, 288.2 eV). After sunlight treatments, the content of carbon bonded to oxygen significantly decreases, confirming the removal of OCGs. The reduction degree is tunable; the increase in solar irradiation intensity directly leads to the removal of more OCGs. Notably, the content of oxygen atoms in pristine GO is as high as 33.4%, while the content of carbon not bonded to oxygen is only 44% (Figure 3e). After sunlight photoreduction, the C—C percentage of RGO-1 increases to 66.5%; the C—O percentage decreases to 29.3%, indicating the removal of OCGs. An increase in the solar radiation intensity would lead to the further reduction of the RGO. The C—C percentage of the RGO-2 sample increased to ≈80% after thorough photoreduction. The residual oxygen is most likely contained in functional groups, such as carboxyl, hydroxyl, and epoxy, due to incomplete deoxygenation. We further investigated the conductivity change after sunlight reduction. As shown in Figure 3f, GO is almost insulating. However, after photoreduction, the current–voltage (I–V) curves of RGO-1 and RGO-2 samples (1 mm × 5 mm) exhibit linear dependence, confirming their good Ohmic contact and tunable conductivity. Obviously, the greater the solar radiation intensity, the smaller the resistance will become. The conductivity of the RGO-2 sample is approximately nine times higher than that of the RGO-1 sample.

Interestingly, the conductivity of these RGO films is highly sensitive to environmental humidity, which becomes a gateway between the digital and physical worlds. We fabricated the humidity-sensing devices using RGO-1 and RGO-2 samples as sensing materials. **Figure 4** shows the systematic characterization of the sensitivity, humidity hysteresis, and cycling performance of our humidity sensors based on RGO-1 and RGO-2 samples. The impedance of the RGO-1 sensor was investigated at different frequencies only while increasing the RH from 11% to 95% at room temperature (Figure 4a). The impedance decreases remarkably with increasing frequency at low RH (11%) and becomes gradually smaller as RH increases. The

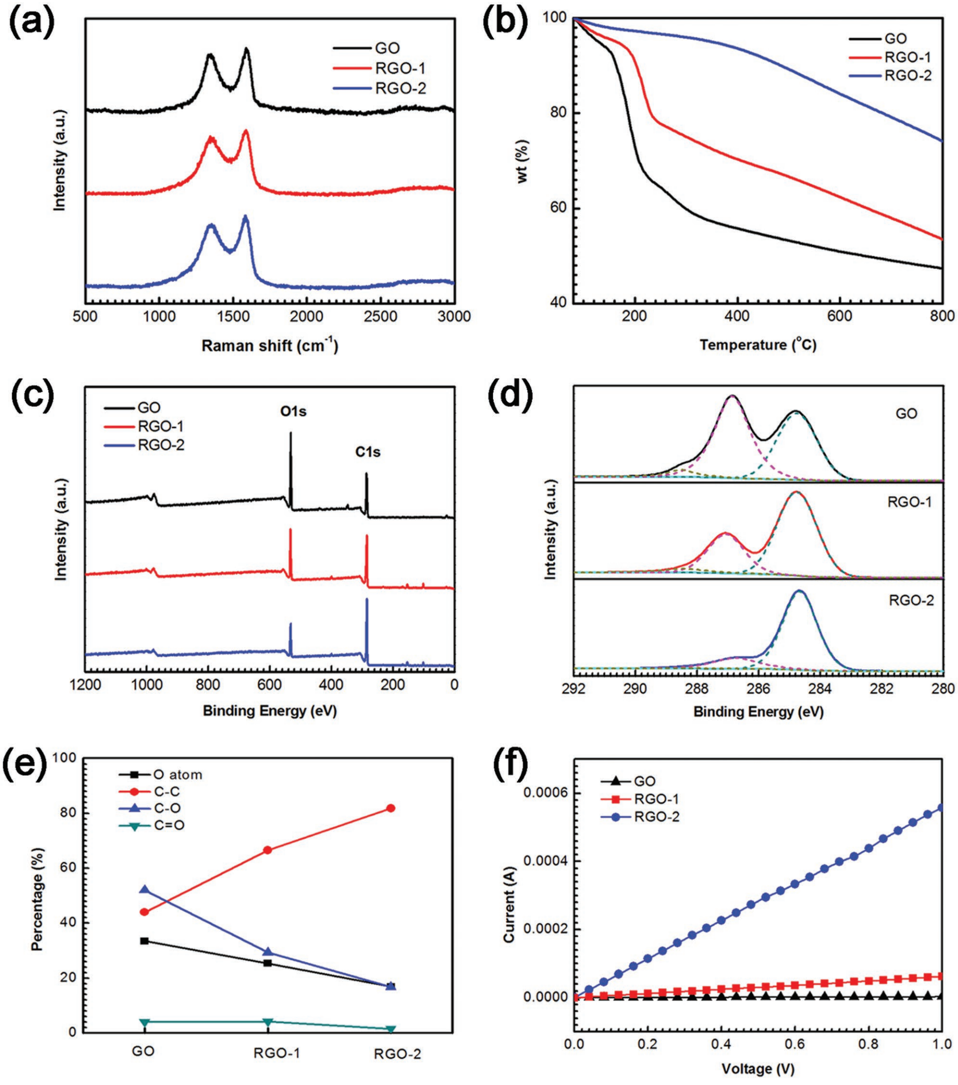

Figure 3. Characterization of GO and RGO samples. a) Raman spectra, b) TG curves, c) Survey XPS spectra and d) C1s XPS spectra of pristine GO, RGO-1, and RGO-2 samples. e) The contents of C—C, C—O, C=O, and O atom percentage of GO, RGO-1, and RGO-2 samples. f) Current–voltage of pristine GO, RGO-1, and RGO-2 samples.

impedance versus RH curve shows good linearity at 20 Hz, with a resistance change of almost three orders of magnitude with the relative humidity changing from 11% to 95%, indicating the high sensitivity.

Figure 4b provides the characteristic humidity hysteresis at room temperature of model humidity sensors constructed from GO, RGO-1, and RGO-2. The upper line corresponds to the adsorption process, while the lower one represents the desorption process. The hysteresis behaviors of RGO-1 and RGO-2 are different since the two samples have different oxygen residuals. Notably, the GO sample is nonresponsive to the change of RH; the resistance for GO remains almost the same over the entire RH range. This nonresponsiveness can be attributed to the insulating properties of GO. In addition, the curves of the RGO-1 device present good linearity and a small hysteresis of ≈11%, showing its good sensitivity. In regard to the RGO-2 device, the linearity of its resistance versus % RH deteriorates over a wide humidity range, with a small hysteresis of ≈9%, and the range of the resistance decreases (only one order of magnitude), which is related to its relatively higher conductivity compared with that of RGO-1.

In addition, the dynamic experiment results exhibited in Figures 4c,d reveal the high cycling behavior (varied only slightly over three cycles) and well-defined response kinetics of the sensing process. Generally, the response and recovery times are defined as the times taken by a sensor to reach 90% of the total impedance change and return to 10% above the original conductance. For the RGO-1 sensors, the response and recovery times are only ≈16 s and ≈47 s, respectively. For the RGO-2 sensors, the response time is ≈18 s, and the recovery time is ≈14 s, indicating a fast response. In particular, the modulation of the oxygen group content grants the opportunity to controlling the adsorption/desorption behavior of water molecules, contributing to the tunable response/recovery times. The presence of OCGs makes RGO-1 more hydrophilic; H-bonding would form between water molecules and RGO-1 sheets in the presence of

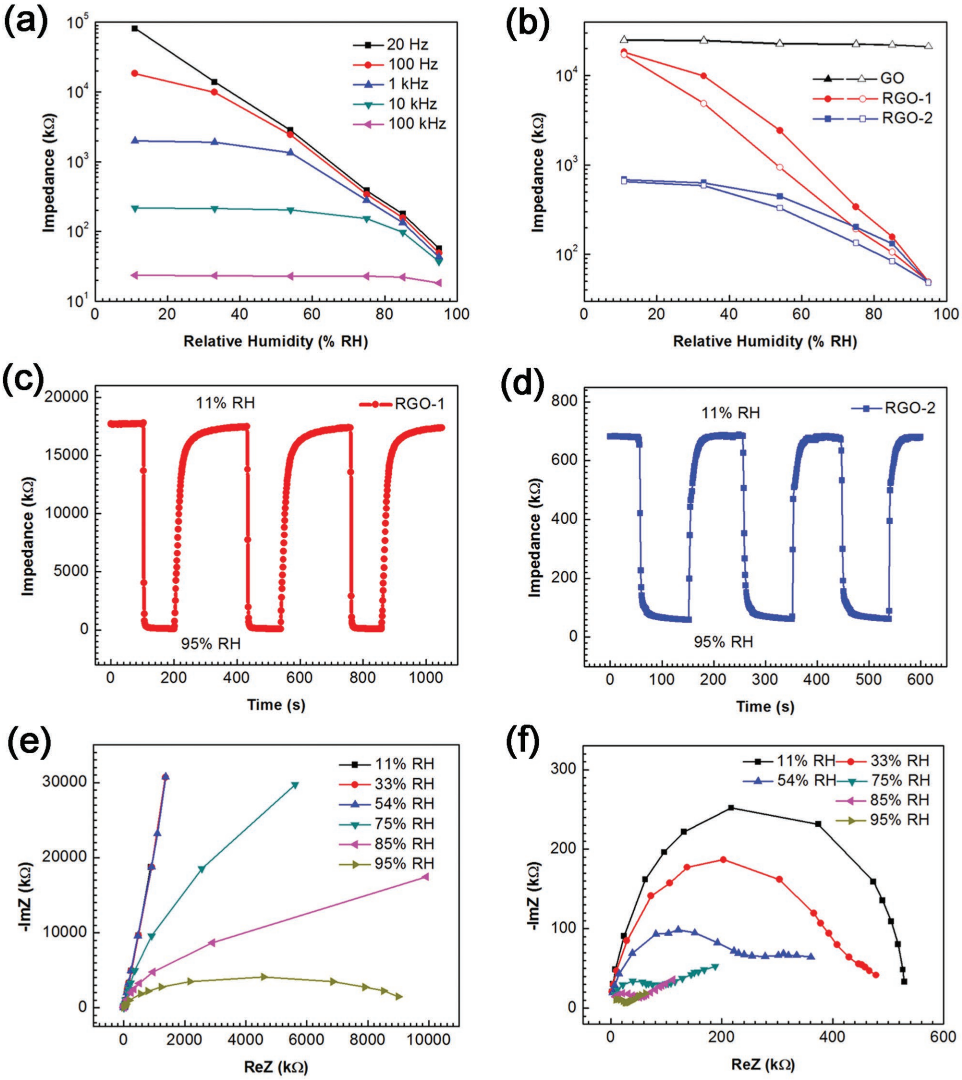

Figure 4. Humidity sensitive properties and sensing mechanism. a) The impedances of the RGO-1 sensor as a function of RH measured at various frequencies. b) The humidity hysteresis plots of GO, RGO-1, and RGO-2 sensors. Response and recovery curves of the c) RGO-1 and d) RGO-2 sensors for three cycles. Complex impedance plots of the e) RGO-1 and f) RGO-2 sensors at various RH.

moisture. Whereas with RGO-2, which has fewer OCGs, the adsorption of water molecules occurs mostly due to the much weaker van der Waals forces. In this regard, the RGO-1 sensor spends less response time in the adsorption process and more recovery time in the desorption process, whereas the RGO-2 sensor has a relatively long response time and a short recovery time.

To gain further insight into the sensing mechanisms at various RH values, we used complex impedance plots (CIPs) to interpret the conductivity and polarization processes of the RGO-1 and RGO-2 sensors in the presence of water molecules. Typical CIPs of the sensor were measured over a frequency range of 20 Hz–100 kHz at different RH values, as demonstrated in Figure 4e. At low RH (11%, 33%, 54%), the CIP is an arc with large curvature radius, which looks like a straight line. At this point, the water vapor is minimal. Hence, only a few water molecules are physically adsorbed on the available active sites (hydrophilic groups, vacancies) of the RGO surfaces, which explains the high sensitivity even at low RH. In this regime, the main conductive particles are protons (H^+). The hopping transfer of protons between adjacent hydroxyl groups requires much energy due to the restriction from hydrogen bonding, which results in comparatively high impedance. As the RH increases to 95%, more water molecules are adsorbed that can be ionized under an electrostatic field to produce a large number of hydronium ions (H_3O^+) synchronously, and a semicircle is observed from the CIP. According to the ion transfer mechanism of the Grotthuss chain reaction ($H_2O + H_3O^+ \rightarrow H_3O^+ + H_2O$), the easy transfer of H_3O^+ leads to the quick decrease in impedance. However, there are many differences in the CIPs of RGO-2 sensors (Figure 4f). At the low RH levels of 11% and 33%, semicircles are observed, which are similar to the result shown in Figure 4e. As the RH further increases to 54%, the CIP consists of most of a semicircle at the high frequency range and a short line at the low frequency range. The curvature of the semicircle decreases along with the

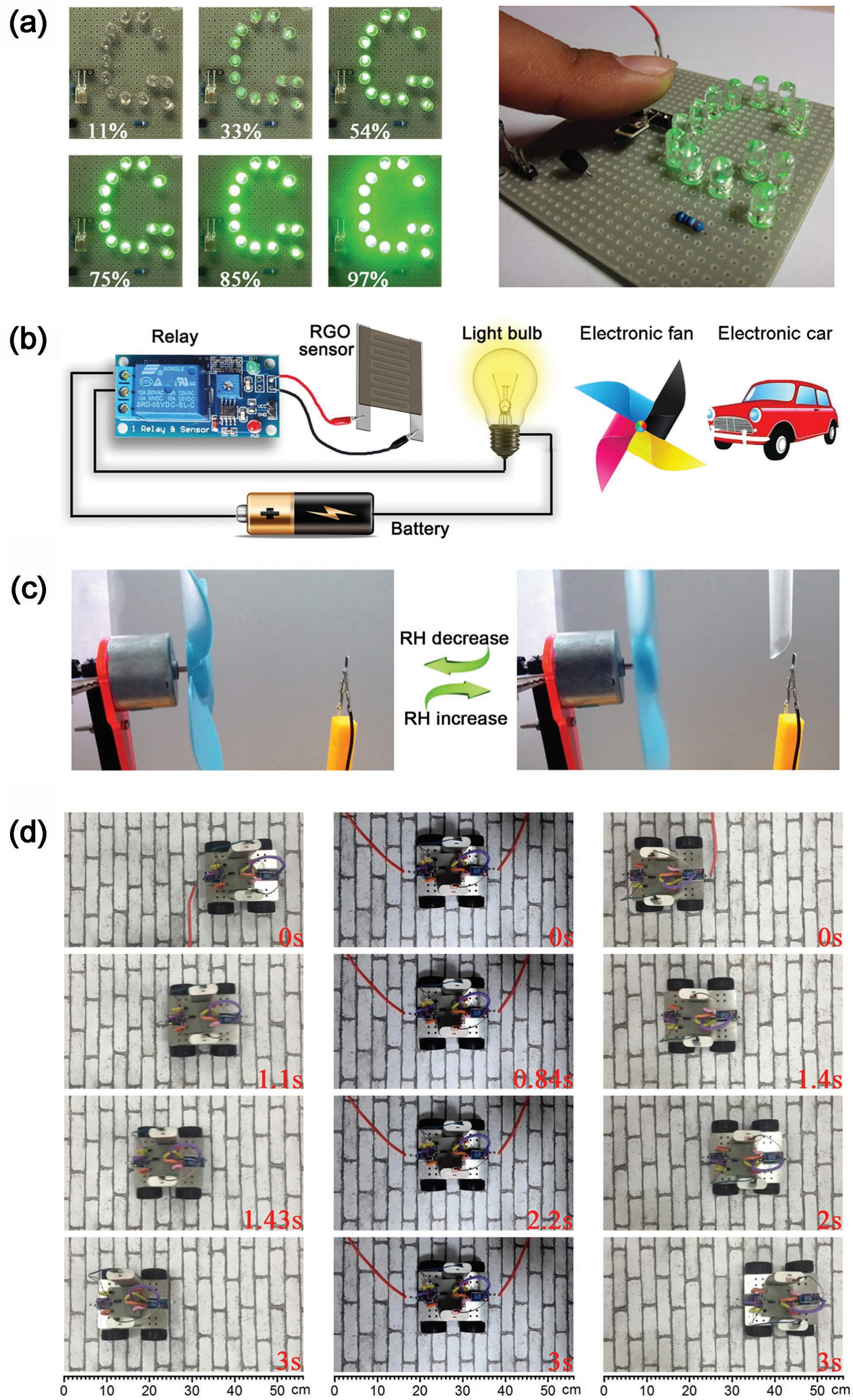

Figure 5. RGO sensor for controlling circuit applications. a) Humidity monitor in dry and moisture conditions. b) Schematic illustration of the design of RGO sensor-enabled smart devices. The bulb could be replaced by different devices such as an electronic fan or car. c) Moisture controller. d) Self-controlled moisture sensing device with an RGO sensor and a car as functional components.

RH increase because the adsorbed water molecules penetrate into the interlayer of the RGO-2 films, which is very beneficial for the partial hydrolysis of the remaining functional groups (carboxyl and/or hydroxyl) on the RGO-2 films, and these ions contribute to the ionic conductivity. The short line represents Warburg impedance, which is caused by the diffusion process of ions or charge carriers at the interface between sensing films and electrodes. To evaluate their long-term stability, RGO-1 and RGO-2 sensors placed into a glass container at 95% RH for repeated measurements every 5 d for 30 d (Figure S2, Supporting Information). The RGO-1 and RGO-2 sensors exhibit very good humidity stability and durability; only a slight variation in impedance could be observed.

As described above, the resistance of the RGO samples is very sensitive to environmental humidity; even a small RH value change will be converted into a digital signal. Therefore, the samples could be applied to a control circuit (Figures S3 and S4, Supporting Information). As shown in **Figure 5**a, when a moisture gas was sprayed onto the RGO-1 sensor, the resistance of the RGO-1 sensor decreased and the Light Emitting Diode (LED) brightened immediately. The on/off state of the LED is a signal of humidity change. When the moisture gas was shut off, the LED turned off rapidly due to water desorption-induced recovery of resistance. Interestingly, the RGO sensor is so sensitive to humidity that it could "turn on" the LED when approaching a human finger. Based on these sensitive RGO humidity sensors, we designed and fabricated a series of intelligent humidity-sensing devices. Figure 5b shows the design sketch of our RGO humidity sensor-enabled smart devices. As a typical example, we employed a fan in the control circuit; in this way, a moisture controller was proposed (Figure 5c). When the ambient humidity increased, it could be turned on, and the strong wind from the fan would immediately promote water molecule desorption and turn off the fan. In this way, the RGO sensor could be integrated with a control circuit that could be used for the maintenance of a certain humidity.

In addition, inspired by the hygrotaxis of earthworms that move to water when in a dry environment, we demonstrated a smart moisture detector with the help of our RGO sensor. As shown in Figure 5d, we integrated two RGO sensors at two opposite ends with a control circuit that can control the motor of a car to move toward different directions. When the RH of the left side increases, the car goes left, rapidly. In contrast, the car will drive to the right when a moisture gas is sprayed from the right side (Videos S1–S3, Supporting Information). In this regard, the sensitive RGO sensor may hold great promise for the development of smart robots that can recognize humidity from different directions and spatially seek out water sources similar to a smart "earthworm."

In addition, due to the fast response and recovery times, the RGO sensor could also be used for other humidity-sensing devices. In this work, we demonstrated an electronic "harmonica" based on our humidity sensors. Unlike a standard harmonica that is played by the airflow from a mouth, our electronic "harmonica" is played by recognizing the humidity of breath. It was prepared by assembling seven RGO sensors into a linear array. As shown in **Figure 6**a, by blowing humidity to each RGO sensor, the control circuit will trigger a buzzer and make a relative sound (e.g., do, re, mi, fa, sol, la, si, Figure 6b). Interestingly, it can even play the famous "Little Star" (Figure 6c; Video S4, Supporting Information), indicating the feasibility of our electronic "harmonica." From this point of view, the facile fabrication of the RGO-based sensor is capable of both moisture recognition and control; it may open up a novel avenue to produce versatile sensing devices.

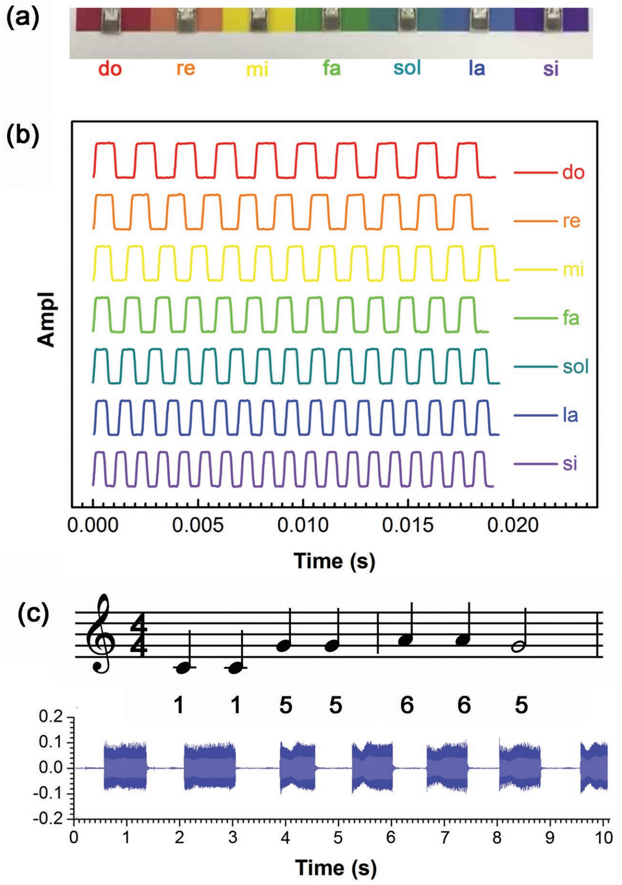

Figure 6. Electronic "harmonica." a) A scheme of harmonica for humidity control. b) The different frequencies of every syllable, 521 Hz (do), 589 Hz (re), 657 Hz (mi), 694 Hz (fa), 788 Hz (sol), 875 Hz (la), and 995 Hz (si). c) "Little Star."

3. Conclusion

In conclusion, focused sunlight-induced photoreduction of GO has been successfully developed toward the facile fabrication of RGO-based humidity-sensing devices. Compared with other RGO-based sensors, the present work is distinguished since it does not require special instruments or complex procedures. The whole fabrication process is very simple and green. The sunlight photoreduction of GO is not only controllable in terms of reduction degree but also benefits the formation of a highly porous nanostructure. The obtained RGO films present tunable electrical conductivity such that they can serve as moisture-responsive films for sensing applications. The humidity sensors based on the RGO samples reveal good sensing performance and excellent stabilities. The sensitive RGO film has been further applied to a control circuit for moisture recognition and control. As a cost-effective and ecofriendly approach to functional RGO, the sunlight-mediated photoreduction of GO holds great promise for the development of versatile humidity-sensing devices.

4. Experimental Section

Sunlight Photoreduction of GO Films: The incident solar radiation was focused on the surface of the GO film using a 60 mm diameter convex lens (focal length = 15 cm, focused spot diameter ≈1 mm). The scanning step length (the distance between two neighboring scanning paths) was ≈0.5 mm. The experiments were performed during April and May (weather: sunshine; time: 8:00–10:00 pm) in the city of Chanchun, which is at a longitude of 125° east and at a latitude of 43° north. The average solar radiation intensities in the range of 280–330 nm were measured to be ≈570 and 710 μW cm^{-2}. To guide the scanning path of the focal spot in a controlled manner, a 2D movable platform with a movement rate at 0.2 mm s^{-1} was used for the GO reduction.

Fabrication and Measurement of Humidity Sensors: A thin film of pristine GO dispersed in water was drop-cast onto a ceramic substrate (6 mm × 3 mm, 0.5 mm in thickness) with five pairs of Ag–Pd interdigitated electrodes (electrode width and distance: 0.15 mm) to form a sensing film. GO papers were reduced using a sunlight reducing method. The characteristic curves of humidity sensitivity were measured on a ZL-5 model LCR analyzer (Shanghai, China). The voltage applied in our studies was AC 1 V, and the frequency varied from 20 Hz to 100 kHz. The controlled humidity environments were achieved using saturated aqueous solutions of LiCl, $MgCl_2$, $Mg(NO_3)_2$, NaCl, KCl, and KNO_3 in a closed glass vessel at an ambient temperature of 25 °C, which yielded ≈11%, 33%, 54%, 75%, 85%, and 97% relative humidity, respectively. The uncertainty of the RH values was ≈±1%. As three-phase (vapor–liquid–solid) systems, saturated salt solutions are free of changes in their total moisture content, which does not have a time delay.[18]

Supporting Information

Supporting Information is available from the Wiley Online Library or from the author.

Acknowledgements

The authors would like to acknowledge the National Natural Science Foundation of China under grant nos. 61522503, 61376123, 61590930, 61377048, and 61435005 for support.

Conflict of Interest

The authors declare no conflict of interest.

Keywords

environmental sensors, graphene, materials science, porous structure, sunlight

Received: February 13, 2017
Revised: March 21, 2017

[1] a) D. D. Han, Y. L. Zhang, J. N. Ma, Y. Q. Liu, B. Han, H. B. Sun, *Adv. Mater.* **2016**, *28*, 8328; b) Y. L. Sun, W. F. Dong, R. Z. Yang, X. Meng, L. Zhang, Q. D. Chen, H. B. Sun, *Angew. Chem., Int. Ed.* **2012**, *51*, 1558; c) J. D. Kim, J. S. Heo, T. Park, C. Park, H. O. Kim, E. Kim, *Angew. Chem., Int. Ed.* **2015**, *54*, 5869; d) T. Park, J. Na, B. Kim, Y. Kim, H. Shin, E. Kim, *ACS Nano* **2015**, *9*, 11830.

[2] a) F. Zhao, Y. Zhao, H. H. Cheng, L. T. Qu, *Angew. Chem., Int. Ed.* **2015**, *54*, 14951; b) H. Shin, S. Seo, C. Park, J. Na, M. Han, E. Kim, *Energy Environ. Sci.* **2016**, *9*, 117; c) Y. Wang, T. T. Yang, J. C. Lao, R. J. Zhang, Y. Y. Zhang, M. Zhu, X. Li, X. B. Zang, K. L. Wang, W. J. Yu, H. Jin, L. Wang, H. W. Zhu, *Nano Res.* **2015**, *8*, 1627.

[3] a) S. Hong, M. Y. Lee, A. O. Jackson, L. P. Lee, *Light: Sci. Appl.* **2015**, *4*, 7; b) J. H. Son, B. Cho, S. Hong, S. H. Lee, O. Hoxha, A. J. Haack, L. P. Lee, *Light: Sci. Appl.* **2015**, *4*, 7; c) H. Zhang, *ACS Nano* **2015**, *9*, 9451.

[4] a) H. Ota, K. Chen, Y. J. Lin, D. Kiriya, H. Shiraki, Z. B. Yu, T. J. Ha, A. Javey, *Nat. Commun.* **2014**, *5*, 9; b) P. Wang, L. Zhang, Y. N. Xia, L. M. Tong, X. Xu, Y. B. Ying, *Nano Lett.* **2012**, *12*, 3145; c) T. T. Yang, W. Wang, H. Z. Zhang, X. M. Li, J. D. Shi, Y. J. He, Q. S. Zheng, Z. H. Li, H. W. Zhu, *ACS Nano* **2015**, *9*, 10867.

[5] a) M. B. Zakaria, C. L. Li, Q. M. Ji, B. Jiang, S. Tominaka, Y. Ide, J. P. Hill, K. Ariga, Y. Yamauchi, *Angew. Chem., Int. Ed.* **2016**, *55*, 8426; b) H. Kim, J. H. Seo, E. Y. Park, T. D. Kim, K. Lee, K. S. Lee, S. Cho, A. J. Heeger, *Appl. Phys. Lett.* **2010**, *97*, 3; c) W. Xiong, Y. Liu, L. J. Jiang, Y. S. Zhou, D. W. Li, L. Jiang, J. F. Silvain, Y. F. Lu, *Adv. Mater.* **2016**, *28*, 2002.

[6] a) Z. Lin, X. H. Ye, J. P. Han, Q. Chen, P. X. Fan, H. J. Zhang, D. Xie, H. W. Zhu, M. L. Zhong, *Sci. Rep.* **2015**, *5*, 7; b) W. Xiong, Y. S. Zhou, W. J. Hou, L. J. Jiang, Y. Gao, L. S. Fan, L. Jiang, J. F. Silvain, Y. F. Lu, *Sci. Rep.* **2014**, *4*, 6; c) D. D. Han, Y. L. Zhang, H. B. Jiang, H. Xia, J. Feng, Q. D. Chen, H. L. Xu, H. B. Sun, *Adv. Mater.* **2015**, *27*, 332; d) D. D. Han, Y. L. Zhang, Y. Liu, Y. Q. Liu, H. B. Jiang, B. Han, X. Y. Fu, H. Ding, H. L. Xu, H. B. Sun, *Adv. Funct. Mater.* **2015**, *25*, 4548.

[7] a) P. Z. Sun, K. L. Wang, H. W. Zhu, *Adv. Mater.* **2016**, *28*, 2287; b) S. Nam, I. Choi, C. C. Fu, K. Kim, S. Hong, Y. Choi, A. Zettl, L. P. Lee, *Nano Lett.* **2014**, *14*, 5584; c) X. Huang, X. Y. Qi, F. Boey, H. Zhang, *Chem. Soc. Rev.* **2012**, *41*, 666; d) H. B. Jiang, Y. L. Zhang, Y. Zhang, Y. Liu, X. Y. Fu, Y. Q. Liu, C. D. Wang, H. B. Sun, *Sci. Rep.* **2015**, *5*, 8.

[8] a) S. Ida, *Bull. Chem. Soc. Jpn.* **2015**, *88*, 1619; b) R. Rajendran, L. K. Shrestha, R. M. Kumar, R. Jayavel, J. P. Hill, K. Ariga, *J. Inorg. Organomet. Polym. Mater.* **2015**, *25*, 267; c) X. Y. Zhang, S. H. Sun, X. J. Sun, Y. R. Zhao, L. Chen, Y. Yang, W. Lu, D. B. Li, *Light: Sci. Appl.* **2016**, *5*, 7.

[9] a) J. Wu, J. Yang, Y. Huang, H. Li, Z. Fan, J. Liu, X. Cao, X. Huang, W. Huang, H. Zhang, *Adv. Mater. Technol.* **2017**, *2*, 1600231; b) Y. Xu, A. Ali, K. Shehzad, N. Meng, M. Xu, Y. Zhang, X. Wang, C. Jin, H. Wang, Y. Guo, *Adv. Mater. Technol.* **2017**, *2*, 1600241; c) Y. Huang, Y. Fang, Z. Zhang, L. Zhu, M. Sun, *Light: Sci. Appl.* **2014**, *3*, e199.

[10] a) V. Georgakilas, J. N. Tiwari, K. C. Kemp, J. A. Perman, A. B. Bourlinos, K. S. Kim, R. Zboril, *Chem. Rev.* **2016**, *116*, 5464; b) D. Qu, M. Zheng, J. Li, Z. G. Xie, Z. C. Sun, *Light: Sci. Appl.* **2015**, *4*, 8.

[11] Q. M. Ji, I. Honma, S. M. Paek, M. Akada, J. P. Hill, A. Vinu, K. Ariga, *Angew. Chem., Int. Ed.* **2010**, *49*, 9737.

[12] K. K. Sadasivuni, A. Kafy, L. D. Zhai, H. U. Ko, S. Mun, J. Kim, *Small* **2015**, *11*, 994.

[13] X. W. Wang, Z. P. Xiong, Z. Liu, T. Zhang, *Adv. Mater.* **2015**, *27*, 1370.

[14] L. Guo, H. B. Jiang, R. Q. Shao, Y. L. Zhang, S. Y. Xie, J. N. Wang, X. B. Li, F. Jiang, Q. D. Chen, T. Zhang, H. B. Sun, *Carbon* **2012**, *50*, 1667.

[15] V. A. Smirnov, A. A. Arbuzov, Y. M. Shul'ga, S. A. Baskakov, V. M. Martynenko, V. E. Muradyan, E. I. Kresova, *High Energy Chem.* **2011**, *45*, 57.

[16] a) K. Shehzad, T. Shi, A. Qadir, X. Wan, H. Guo, A. Ali, W. Xuan, H. Xu, Z. Gu, X. Peng, *Adv. Mater. Technol.* **2017**, *2*, 1600262; b) C. F. Guo, T. Sun, F. Cao, Q. Liu, Z. Ren, *Light: Sci. Appl.* **2014**, *3*, e161; c) K. Lee, J. Lee, B. A. Mazor, S. R. Forrest, *Light: Sci. Appl.* **2015**, *4*, e288; d) V. Eswaraiah, S. S. J. Aravind, S. Ramaprabhu, *J. Mater. Chem.* **2011**, *21*, 6800; e) T. S. Wu, S. Liu, H. L. Li, L. Wang, X. P. Sun, *J. Nanosci. Nanotechnol.* **2011**, *11*, 10078.

[17] a) M. Mohandoss, S. S. Gupta, A. Nelleri, T. Pradeep, S. M. Maliyekkal, *RSC Adv.* **2017**, *7*, 957; b) W.-C. Hou, I. Chowdhury, D. G. Goodwin Jr., W. M. Henderson, D. H. Fairbrother, D. Bouchard, R. G. Zepp, *Environ. Sci. Technol.* **2015**, *49*, 3435.

[18] a) L. Greenspan, *J. Res. Natl. Bur. Stand., Sect. A* **1977**, *81A*, 1; b) L. B. Rockland, *Anal. Chem.* **1960**, *32*, 10; c) D. Kitic, D. C. P. Jardim, G. J. Favetto, S. L. Resnik, J. Chirife, *J. Food Sci.* **1986**, *51*, 1037.